



UNIVERSITY OF WATERLOO
FACULTY OF MATHEMATICS

Timothy Thompson, BAsC Mechanical Engineering

Simulating Failure of Cortical Bone With an Energy Based Discrete Fracture Model

Research Paper

to achieve the University degree of

Master of Mathematics

Master's degree program: Computational Mathematics

submitted to

University of Waterloo

Supervisor

Dr.Katerina D. Papoulia

August 2019

This document is set in Palatino, compiled with [pdfL^AT_EX2e](#) and [Biber](#).

The L^AT_EX template from Karl Voit is based on [KOMA script](#) and can be found online: <https://github.com/novoid/LaTeX-KOMA-template>

Affidavit

I declare that I have authored this thesis independently, that I have not used other than the declared sources/resources, and that I have explicitly indicated all material which has been quoted either literally or by content from the sources used.

Acknowledgments: This project builds upon the PhD Thesis work of Dr. Mohammed Hirmad Reza. The supervisor for my Master's thesis and this project was Professor Katerina D. Papoulia. The ADMM method presented in this paper was introduced to the group's efforts by James Petrie.

Abstract

This project studies simulation of human cortical bone at the osteon level and at the macroscale. The model used is an energy based approach to generalized cohesive fracture. A two-field discontinuous Galerkin finite element method is used which treats the displacement field and crack opening displacements as separate variables. In contrast to Newtonian approaches, the explicit minimization of the material energy consisting of bulk and cohesive parts allows for a smooth transition of material points from the undamaged to the cohesive state in the sense that the nodal forces are continuous functions of the displacements. The approach results in a non-differentiable, non-convex constrained optimization problem that is solved with a block coordinate descent algorithm. Comparison is made to available results in the literature. In addition, an adjusted model has been prepared which allows for the representation of anisotropic material response at the macroscale. Comparison is made with experimental results and with distributed modeling of fracture using a damage model.

Contents

Abstract	v
1 Introduction	1
2 Energy Based Method to Computational Fracture	3
2.1 Variational Problem	3
2.2 Definition of Cohesive Surface Energy Function	6
2.3 Computational Algorithms	7
2.3.1 ADMM	8
3 Cortical Bone Case Study	11
3.1 Simulation of Meso-scale Features: Osteons	11
3.2 Simulation of Macro-scale Problem: Beam with Notch	27
Bibliography	39

List of Figures

1.1	Schematic image of features in Cortical Bone including an Osteon	2
2.1	Continuum Potato Ω containing internal discontinuity boundary Γ_d	4
2.2	Linear Softening law for tractions	7
2.3	ψ_{coh} and the set of generalized derivatives at 0 opening displacement	8
3.1	Geometry of Single Osteon Model	12
3.2	Schematics of Mixed Boundary Conditions Applied to Single Osteon Model	12
3.3	Single Osteon quadrilateral element FE meshes prepared by Id-kaidek and Jasiuk	14
3.4	Results from each single Osteon coarse mesh.	15
3.5	Results from each single Osteon refined mesh.	16
3.6	Emergence of dominant crack in single Osteon coarse mesh	18
3.7	Process for drawing geometry of Multi-Osteon Model	19
3.8	Schematics of Mixed Boundary Conditions Applied to Multi-Osteon Model	20
3.9	Results of Coarse Mesh Multi-Osteon Geometry; $3 \mu\text{m}$ Boundary Condition	21
3.10	Results of Coarse Mesh Multi-Osteon Geometry; $5 \mu\text{m}$ Boundary Condition	22
3.11	Results of Coarse Mesh Multi-Osteon Geometry; $10 \mu\text{m}$ Boundary Condition	23
3.12	Results of Refined Mesh Multi-Osteon Geometry	24
3.13	Example of meshed cement line with 3-element through the thickness of the cement-line	25
3.14	Principle strain contour for Multi-Osteon mesh with 5222 elements	26
3.15	Principle strain contour for Multi-Osteon mesh with 24329 elements	26
3.16	Principle strain contour for Multi-Osteon mesh with 68325 elements	27
3.17	Test geometry for 3-point bend test of human cortical bone	28
3.18	Results from imaging the microdamage process zone	28

List of Figures

3.19	Microdamage process zone, contour produced from Hashin Fiber Composite model	29
3.20	Differential elements along an interface with material directions \vec{m}_1 \vec{m}_2	30
3.21	Principle Strain Contour of First Test Simulation for Anisotropic extension to Base Model	31
3.22	Principle Strain Contour of Second Test Simulation for Anisotropic extension to Base Model	32
3.23	Principle Strain Contour of Third Test Simulation for Anisotropic extension to Base Model	33
3.24	Force History of First Test Simulation for Anisotropic extension to Base Model	35
3.25	Force History of Second Test Simulation for Anisotropic extension to Base Model	35
3.26	Force History of First Third Simulation for Anisotropic extension to Base Model	36
3.27	Crack paths obtained for Macro-scale problem using Anisotropic extension	37
3.28	Crack paths obtained for Macro-scale problem using Anisotropic extension	38

List of Tables

3.1	Material Properties of Single Osteon Model	13
3.2	Meshes considered for the Single Osteon Case Study	13
3.3	Meshes considered for the Multi-Osteon Case Study	19
3.4	Anisotropic Material Properties used for Test Simulations	31
3.5	Anisotropic Material Properties used for Macro-scale Problem	36

1 Introduction

The fracturing of human bone is an important and not yet fully understood problem. From a clinical perspective many factors of health and demographics have been found to impact risk of bone fracture. However from a mechanics perspective, there is much work to be done in understanding the problems that promote bone fracture. A fracture (a discrete crack in the material) results if an outside force is exerted on a bone such that it exceeds the amount of force the bone can withstand¹. However, bone is a highly complex material with a hierarchical structure² and displays various fracture mechanisms at different length scales.

This problem was brought to the attention of the investigator by literature review and the paper “Cortical bone fracture analysis using XFEM – case study” authored by Ashraf Idkaidek and Iwona Jasiuk³. Cortical bone comprises up to 80 percent of skeletal mass and is a stiff, dense outer layer of bone that protects the internal cavity. It makes up the majority of the weight bearing and structural utility of bone. Within cortical bone, at the mesoscale are several different structures. Figure 1 shows an enlarged view of an Osteon⁴. Osteon have a thin cement line surrounding their circumference adhering them to the matrix of the cortical bone.

¹Wedro, 2017.

²Vashishth, 2007.

³Idkaidek and Jasiuk, 2017.

⁴Singh, 2018.

1 Introduction

Compact Bone & Spongy (Cancellous Bone)

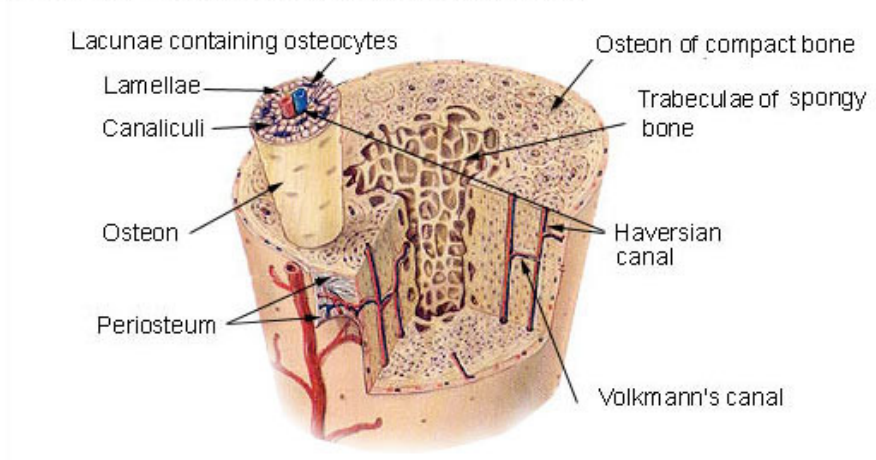


Figure 1.1: Schematic image of features in Cortical Bone including an Osteon.

The objective of this report is to accurately model the fracture in cortical bone at the meso-scale with an energy based discrete fracture approach and compare these results to those of Idkaidek and Jasiuk. In addition, it will be shown at the same method can be used to accurately model the fracture in cortical bone at the macro-scale. Comparison will be made to work by Professor Thomas Willet and his PhD Candidate Daniel Daapah.

2 Energy Based Method to Computational Fracture

2.1 Variational Problem

Consider a linear elastic body $\Omega \subset \mathbb{R}^2$ undergoing infinitesimal deformation, shown in Figure 2.1. The body Ω is bounded externally by $\partial\Omega$ with a unit normal denoted by \mathbf{n} , and contains an evolving internal discontinuity boundary $\Gamma_d \subset \mathbb{R}^1$ with a unit normal \mathbf{n}_d . Displacements \mathbf{u} and external forces \mathbf{t} are prescribed on $\partial_u\Omega$ and $\partial_t\Omega$ such that $\partial_u\Omega \cap \partial_t\Omega = \emptyset$ and $\partial_u\Omega \cup \partial_t\Omega = \partial\Omega$. The task of computational fracture is to obtain a solution for the displacement field $\mathbf{u}(x, t) : \Omega \mapsto \mathbb{R}^2 \times [0, T)$ which a discontinuity on Γ_d denoted by $[[\mathbf{u}(x, t)]]$ on Γ_d and a crack opening field $(x, t) : \Gamma_d \mapsto \mathbb{R}^2 \times [0, T)$. By definition we require that¹

$$[[\mathbf{u}(x, t)]] - \delta(x, t) = 0. \quad (2.1)$$

¹Hirmand and Papoulia, 2019.

2 Energy Based Method to Computational Fracture

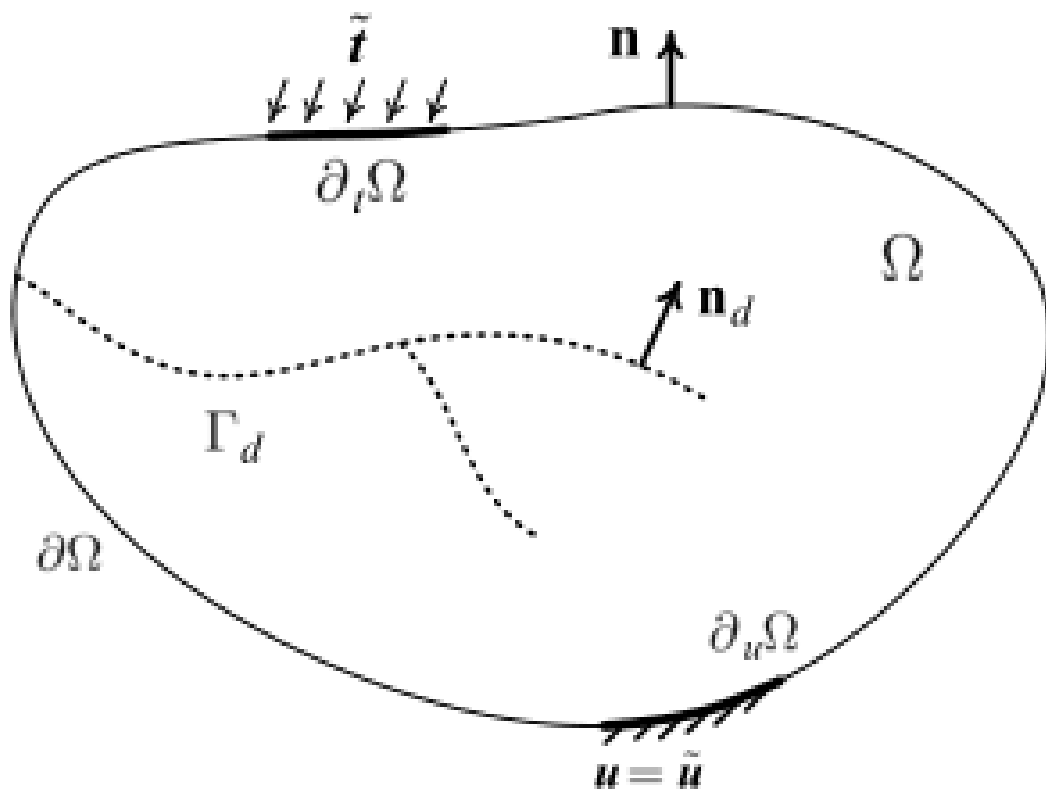


Figure 2.1: Continuum Potato Ω containing internal discontinuity boundary Γ_d .
Reproduced from Hirmand and Papoulia, 2019

2.1 Variational Problem

The energy based method proceeds to solve for the deformation and crack opening fields by considering the minimization of the potential energy of Ω , i.e.

$$\min_{\mathbf{u}, \delta} \{E(\mathbf{u}, \delta) = \varepsilon(\mathbf{u}) + C([\![\mathbf{u}]\!], \delta) - W(\mathbf{u})\} \quad (2.2)$$

Where $\varepsilon(\mathbf{u})$ represents the strain energy due to deformation of the linear elastic material, $C([\![\mathbf{u}]\!], \delta)$ represents the cohesive surface energy due to cracks and $W(\mathbf{u})$ represents the work of external forces. Or in terms of integrals over the region Ω :

$$\varepsilon = \int_{\Omega/\Gamma_d} \psi(\varepsilon(\mathbf{u})) dV \quad (2.3)$$

where $\psi(\varepsilon(\mathbf{u})) = \frac{1}{2} \varepsilon(\mathbf{u}) : \mathbf{D} : \varepsilon(\mathbf{u})$. \mathbf{D} being the elasticity constitutive tensor and $\varepsilon(\mathbf{u}) := \nabla^s \mathbf{u} \in \mathbb{R}^2 \times \mathbb{R}^2$ is the strain tensor.

$$W(\mathbf{u}) = \int_{\Omega/\Gamma_d} \mathbf{u} \cdot \mathbf{b} dV + \int_{\partial_t \Omega} \mathbf{u} \cdot \mathbf{t} dS \quad (2.4)$$

where \mathbf{b} represent any body forces.

$$C([\![\mathbf{u}]\!], \delta) = \int_{\Gamma_d} \psi_{cohs}(\delta) + I_{\mathbb{R}^+}(\delta_n) dS \quad (2.5)$$

where $\psi_{cohs}(\delta)$ is the cohesive surface energy function and $I_{\mathbb{R}^+}(\delta_n)$ is a indicator function at introduces infinite energy for any $\delta_n < 0$ effectively prohibiting interpenetration of crack surfaces.

By posing the above minimization problem as a constrained minimization, the Lagrangian can we written down. The constrained minimization problem is

$$\text{Find } (\bar{\mathbf{u}}, \bar{\delta}) \text{ minimizing } E(\mathbf{u}, \delta) \text{ such that } g(\mathbf{u}, \delta) = 0 \quad (2.6)$$

and

$$g(\mathbf{u}, \delta) = [\![\mathbf{u}(x, t)]\!] - \delta(x, t) \quad (2.7)$$

The Lagrangian of the constrained optimization problem (2.6) is:

2 Energy Based Method to Computational Fracture

$$L(\mathbf{u}, \delta, \lambda) = E(\mathbf{u}, \delta) + \int_{\Gamma_d} \lambda \cdot g(\mathbf{u}, \delta) \quad (2.8)$$

where λ is the Lagrange multiplier field. Saddle points of equation 2.8 correspond to solutions to equation 2.6. In section 2.3 it will be shown how to find saddle point solutions to 2.8 using two different computational algorithms

2.2 Definition of Cohesive Surface Energy Function

What remains to be defined in equation 2.2 is the exact form of the cohesive surface energy, i.e. $\psi_{cohs}(\delta)$ and $I_{\mathbb{R}^+}(\delta_n)$. The form of $\psi_{cohs}(\delta)$ considered here is taken from a irreversible traction-separation law suggested by Ortiz and Pandolfi². First a scalar "effective" opening is defined as

$$\delta = \sqrt{(\delta_n^+)^2 + \beta^2 \|\delta_s\|^2} \quad (2.9)$$

Where $\beta > 0$ is a parameter define to weight the material strength in the normal and tangential directions.

If as suggested by Ortiz and Pandolfi, the tractions along crack surfaces follow a linear softening law as in Figure 2.2, and noting that $t_{cohs} = \frac{\partial \psi_{cohs}}{\partial \delta}$, then it can be shown that $\psi_{cohs}(\delta)$ has the concave quadratic expression shown in equation 2.10.

$$\psi_{cohs}(\delta, \delta_{max}) = \begin{cases} \frac{\sigma_{max} \delta^2}{2\delta_{max}} & \delta \in [0, \delta_{max}) \\ \frac{\sigma_{max} c}{c - \delta_{max}} \left(\delta - \frac{\delta^2}{2\delta_c} = \frac{\delta_{max}}{2} \right) & \delta \in [\delta_{max}, c) \\ \frac{\sigma_{max} \delta_c}{2} & \delta \in [\delta_c, \infty) \end{cases} \quad (2.10)$$

Where δ_{max} is a history variable representing the maximum achieved opening displacement and σ_{max} is the corresponding traction defined by the linear softening law.

²Ortiz and Pandolfi, 1999.

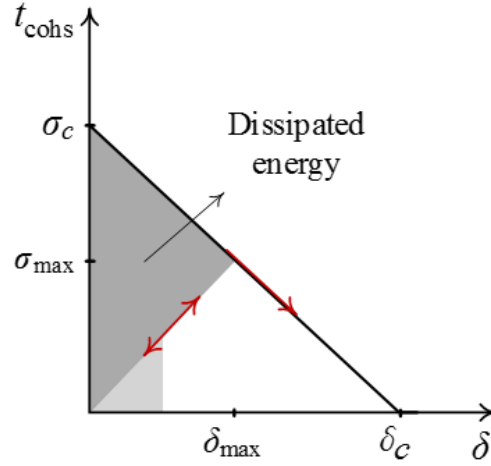


Figure 2.2: Linear Softening law for tractions.

As stated previously $I_{\mathbb{R}^+}(\delta_n)$ is introduced as a interpenetration penalty for the crack surfaces and has the following form:

$$I_{\mathbb{R}^+}(\delta_n) = \begin{cases} \infty & \delta_n \in [-\infty, 0) \\ 0 & \delta_n \in [0, \infty) \end{cases} \quad (2.11)$$

As shown in Figure 2.3, the set of derivatives of ψ_{cohs} at 0 opening displacement is supported by σ_c in the normal direction and σ_c in the tangential direction. These become the material strengths of the material for tensile and shear fracture respectively.

2.3 Computational Algorithms

The first step to obtaining a computational solution to 2.8 is to project the admissible solutions of our field variables down to finite dimensional space. A Discontinuous-Galerkin finite element discretization has been employed. Consider a finite element triangularization of Ω , Ω_h . Then $\Gamma_{d,h}$ is the union of all inter-element boundaries in Ω_h . $\Gamma_{d,h}$ is discretized by 1-D "interface elements". Finite element discretizations for \mathbf{u} and δ are introduced, namely \mathbf{u}_h and δ_h . In this \mathbf{u}_h is represented on each element by quadratic-order elements, and

2 Energy Based Method to Computational Fracture

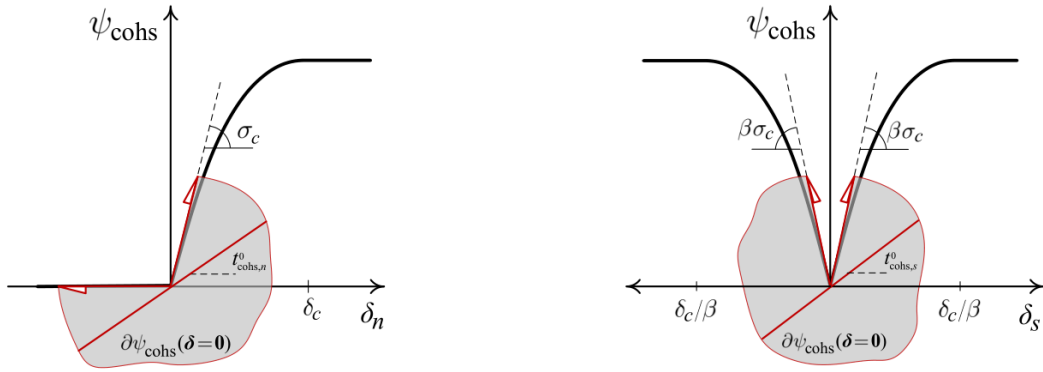


Figure 2.3: ψ_{cohs} and the set of generalized derivatives at 0 opening displacement.
Reproduced from Hirmand and Papoulia, 2019

δ_h is represented by piece-wise constant approximations where the opening displacement is approximated at three Gauss points along each 1-D element.

Two computational algorithms have been identified for the effective solution of equation. Both methods share the characteristic of using a "staggered" scheme where the displacement field and crack openings are solved alternatively, keeping the other constant, until convergence. For problems where dynamic effects are important, the Block Coordinate Descent or "Block-CD" method is best method that has been identified. For problems where dynamics effects can be ignored, i.e. quasi-static problems, the method of Alternating Direction Method of Multipliers is the best method that has been identified.

2.3.1 ADMM

The case study reported in the present work involves only quasis-static problems, so details on the ADMM method are detailed here. In the ADMM method a matrix A is computed which calculates the jump of \mathbf{u} as:

$$A\mathbf{u} = [[\mathbf{u}]] \quad (2.12)$$

The Lagrangian can then be written down by replacing constraint $g(\mathbf{u}, \delta)$ with $A\mathbf{u} - \delta$ and introducing an additional quadratic penalty term with penalty parameter ρ :

$$L(u, \delta, \lambda) = \int_{\Omega/\Gamma_d} \underbrace{\frac{1}{2}u^T K u}_{\text{elastic energy}} dV + \int_{\Gamma_d} \psi(\delta) dS + \int_{\Gamma_d} \lambda^T (Au - \delta) dS \\ + \int_{\Gamma_d} \frac{1}{2} \rho (Au - \delta)^2 dS$$

ADMM solves the Lagrangian minimization by performing a staggered update of the deformation and crack opening field, and updating the Lagrange multiplier field until convergence.

2 Energy Based Method to Computational Fracture

ADMM:

while(not converged)

$$\mathbf{u}^{n+1} := \operatorname{argmin}_{\mathbf{u}} L(\mathbf{u}, \delta, \lambda)$$

$$\delta^{n+1} := \operatorname{argmin}_{\delta} L(\mathbf{u}, \delta, \lambda)$$

$$\lambda := \lambda - \rho * (A\mathbf{u} - \delta)$$

end while

if $\rho > \sigma_c / \delta_c$ both updates can be solved exactly

More details by be found in an upcoming paper published by James Petrie.

3 Cortical Bone Case Study

Idkaidek and Jasiuk studied the mesh sensitivity of two different models of Osteon geometry, whilst using the eXtended Finite Element Method (XFEM) in the commercial software ABAQUS.

3.1 Simulation of Meso-scale Features: Osteons

The first problem studied is simple tensile extension of a single Osteon. Fixed vertical displacement boundary conditions are applied to the nodes on the bottom edge, and fixed vertical and horizontal displacement boundary conditions are applied to the bottom left node. A vertical displacement boundary condition is applied at the top edge with a value of 0.5 micrometres. Following Idkaidek and Jasiuk's terminology, the combination of boundary conditions is referred to as 'Mixed Boundary Conditions'. The single Osteon model is composed of three distinct material regions. Those being the Osteon itself, the interstitial matrix surrounding the Osteon, and the cement line separating the two. Figure 3.1 shows the geometry of the model, and Figure 3.2 shows the 'Mixed Boundary Conditions' applied to the model.

3 Cortical Bone Case Study

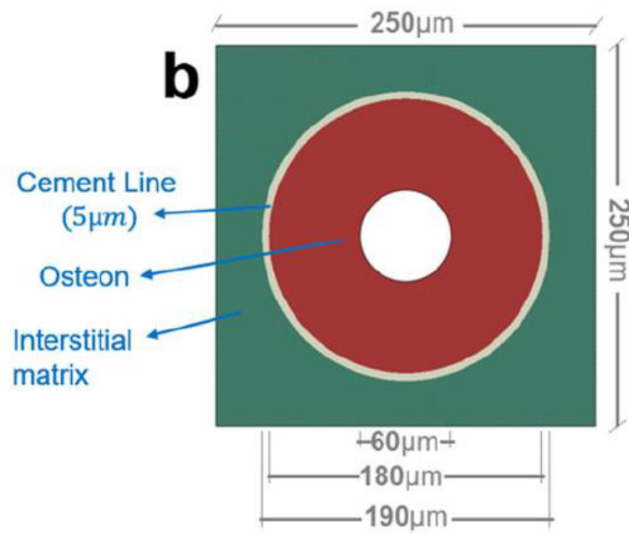


Figure 3.1: Geometry of Single Osteon Model. Reproduced from Idkaidek and Jasiuk, 2017.

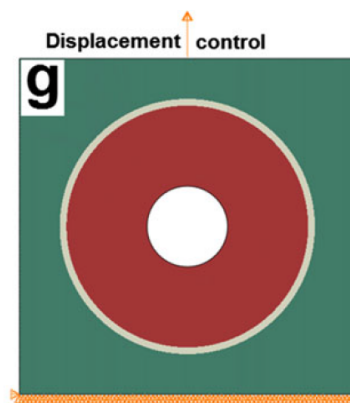


Figure 3.2: Schematics of Mixed Boundary Conditions Applied to Single Osteon Model. Reproduced from Idkaidek and Jasiuk, 2017.

3.1 Simulation of Meso-scale Features: Osteons

Four parameters per material are required in order to define the elastic and fracture response: Young's modulus, poisson's ratio, Griffith's energy release rate and cohesive strength. The former two are given by Idkaidek and Jasiuk, while the latter two are calculated using elementary concepts from fracture mechanics. The Griffith's energy release rate is found as¹:

$$G_c = \frac{(1 - \nu^2)K_{IC}}{E} \quad (3.1)$$

The cohesive strength is calculated based on the failure criteria of maximum principal strain of 0.4%², therefore:

$$\sigma_c = 0.0004 \cdot E \quad (3.2)$$

The material properties for the single Osteon problem are placed in Table 3.1. Idkaidek and Jasiuk prepared four quadrilateral element FE meshes, and the

Material	K_{IC} [MPa · \sqrt{m}]	ν	E [GPa]	G_c [MPa · m]	σ_c [MPa]
Osteon	1.35	0.33	13.50	$12.030 \cdot 10^{-5}$	$5.40 \cdot 10^{-3}$
Matrix	1.46	0.3	14.60	$13.286 \cdot 10^{-5}$	$5.84 \cdot 10^{-3}$
Cement	1.01	0.41	10.12	$8.386 \cdot 10^{-5}$	$4.04 \cdot 10^{-3}$

Table 3.1: Material Properties of Single Osteon Model

results of the two coarsest meshes are considered, shown in Figure 3.3. Idkaidek and Jasiuk used four-node bilinear elements.

Two meshes of similar mesh densities were generated for this project. Table 3.2 below summarizes the meshes considered for the single Osteon case study.

	Idkaidek and Ashraf, 2017	Present Work
Coarse Mesh	2381 (quadrilateral bilinear elements)	3084 (triangular quadratic elements)
Refined Mesh	8304 (quadrilateral bilinear elements)	7454 (triangular quadratic elements)

Table 3.2: Meshes considered for the Single Osteon Case Study

Idkaidek and Jasiuk used three different load increment sizes: 0.05, 0.01 and 0.001, meanwhile the increment sizes using in the present work were: 0.05,

¹Lawn, 1993.

²Idkaidek and Jasiuk, 2017.

3 Cortical Bone Case Study

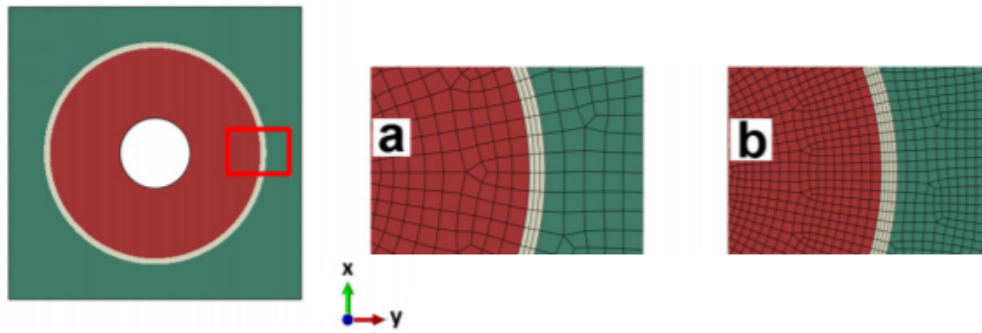


Figure 3.3: Single Osteon quadrilateral element FE meshes prepared by Idkaidek and Jasiuk. Reproduced from Idkaidek and Jasiuk, 2017.

0.01 and 0.005. The important results to be obtained for this problem are the principle strain contours and crack paths at total deformation. Idkaidek and Jasiuk reported strain counters with a deformation scale of 20. The method used in the present work allowed both the strain contours (also plotted here with a deformation scale of 20), and crack paths to be plotted. Figure 3.4 summarizes the results from each coarse mesh. Figure 3.5 summarizes the results from each refined mesh.

3.1 Simulation of Meso-scale Features: Osteons

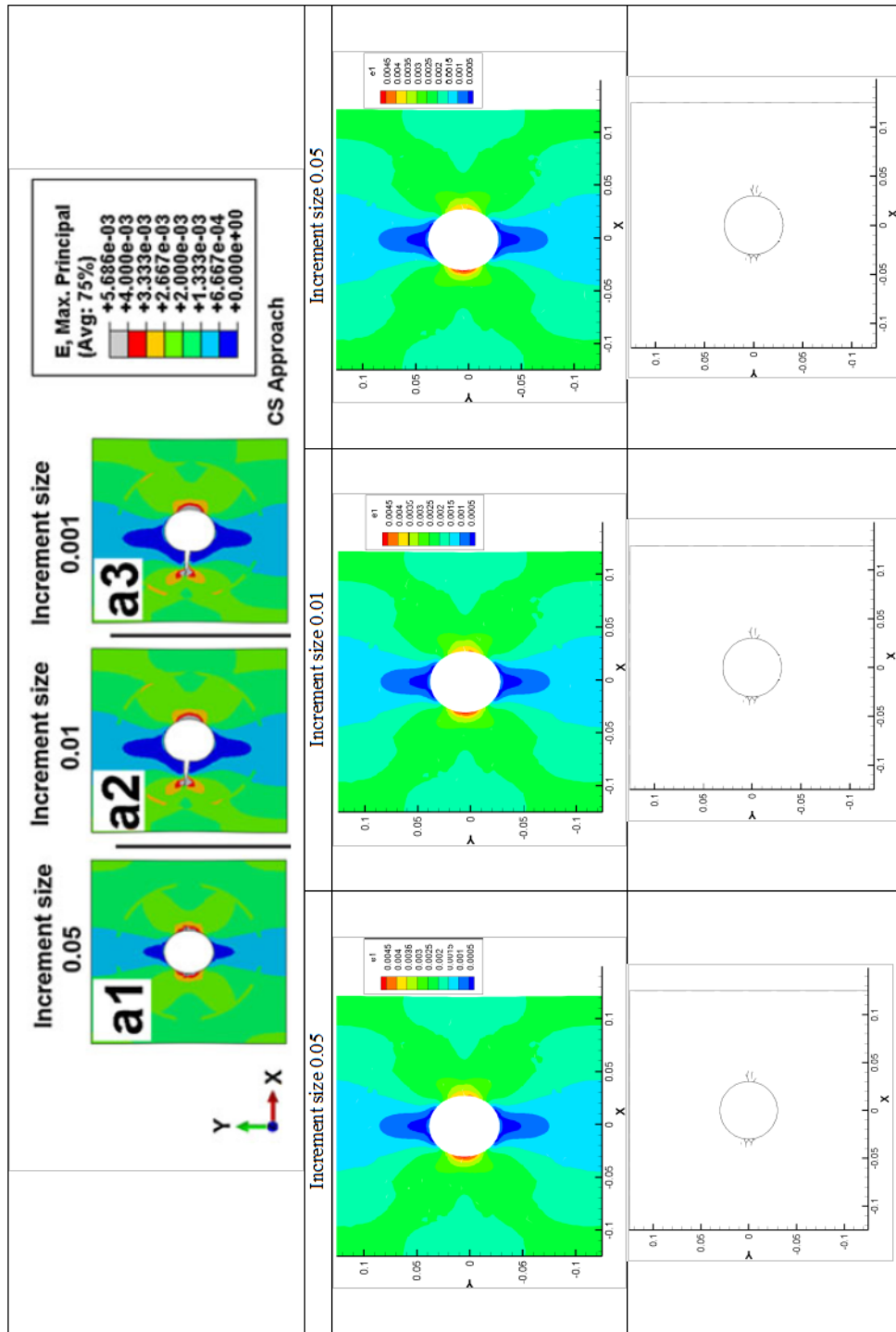


Figure 3.4: Results from each single Osteon coarse mesh. Results reproduced from Idkaidek and Jasiuk, 2017 on top row, results from Present work on middle and bottom row.

3 Cortical Bone Case Study

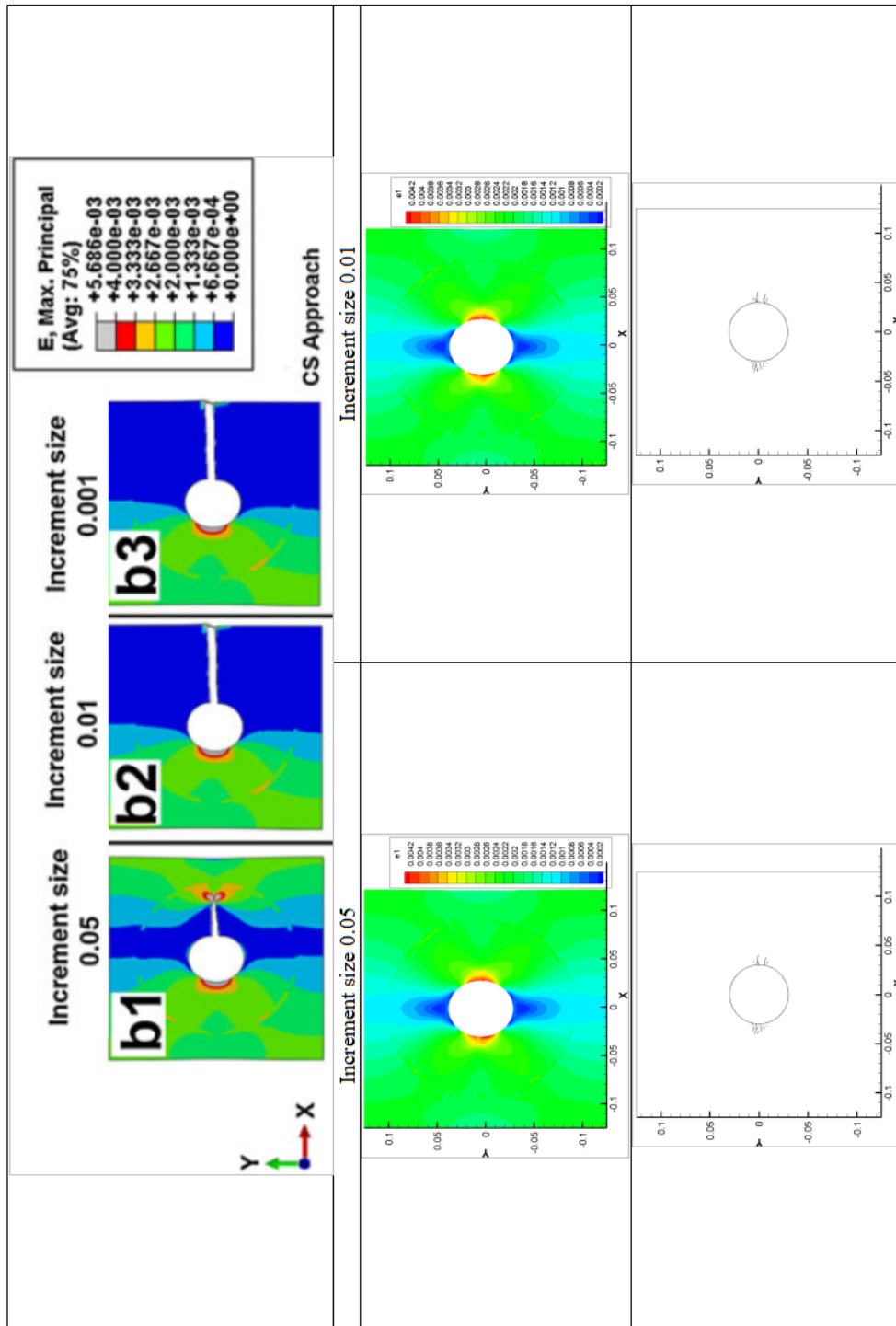


Figure 3.5: Results from each single Osteon refined mesh. Results reproduced from Idkaidek and Jasiuk, 2017 on top row, results from Present work on middle and bottom row.

3.1 Simulation of Meso-scale Features: Osteons

Since the results from the present work formed only narrow cracks compared to the ABAQUS results by Idkaidek and Jusiuk, the fastest model (coarse mesh with 0.05 increment) was pulled until a dominant crack was produced. The crack produced at about 0.8 microns of deformation and these results should be compared to 'b2' and 'b3' in Figure 3.5. Figure 3.6 shows a couple frames of the dominant crack propagating.

The results from the present work show a strong convergence in load increment size, each strain contour and crack path are virtually indistinguishable from their counterparts with different load increment size. The crack path results in Figure 3.4 and Figure 3.5 shows that the the energy based discrete fracture method can provide converged result with large increment steps, at least as large as 0.05. At this time, the results in the present work have not shown a complete convergence with respect to spatial discretization. This is due to the inherent mesh dependence of a discrete crack representation of fracture along element edges. It is expected that refining the mesh further would produce totally convergent results. Taking note of the convergent behavior of the results so far with respect to increment size, more refined meshes need only be tested with 0.05 increment size.

3 Cortical Bone Case Study

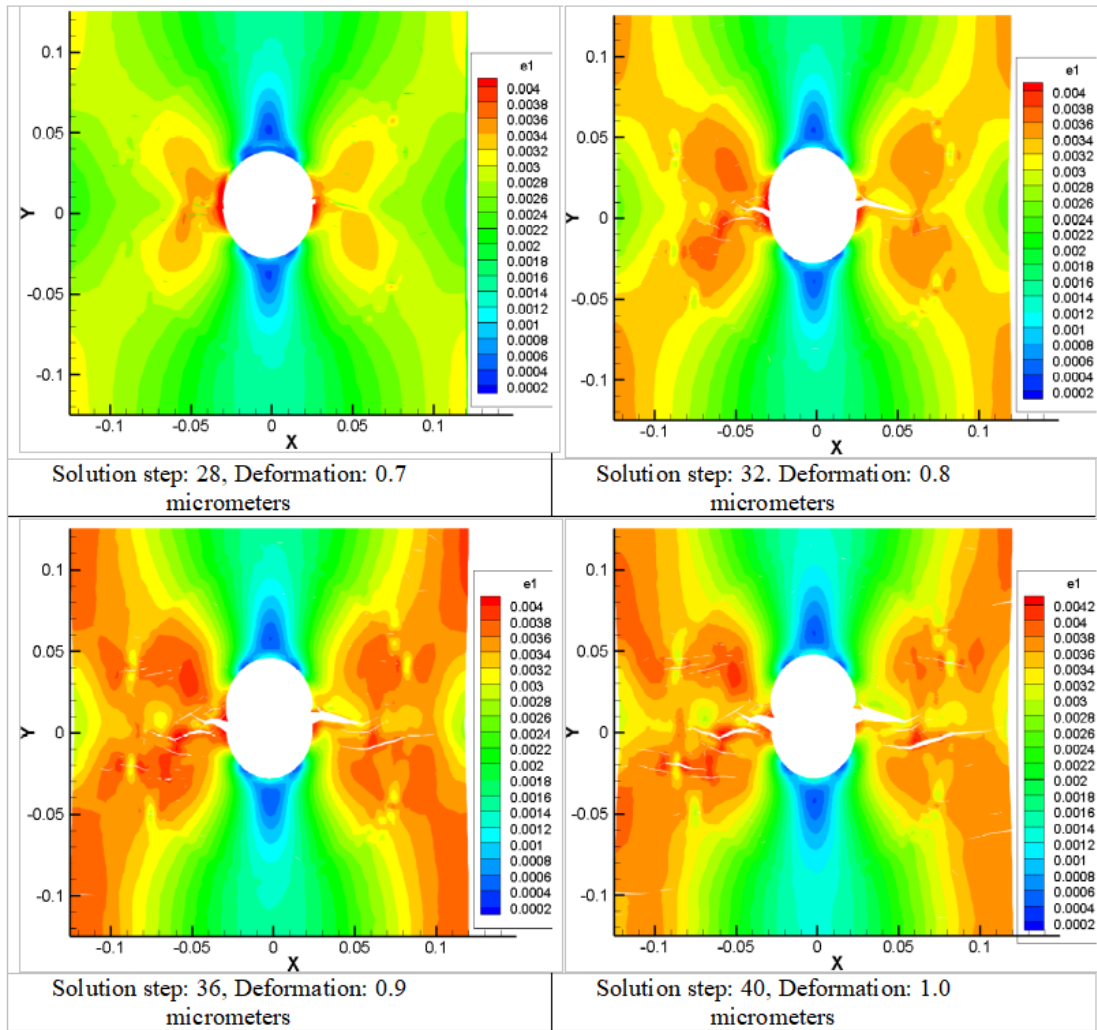


Figure 3.6: Emergence of dominant crack in single Osteon coarse mesh.

3.1 Simulation of Meso-scale Features: Osteons

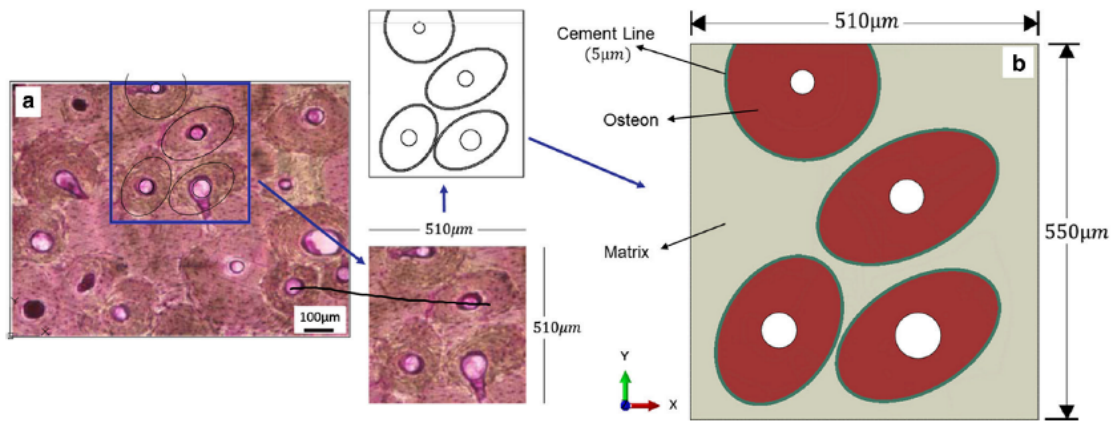


Figure 3.7: Process for drawing geometry of Multi-Osteon Model.
 Reproduced from Idkaidek, Koric, and Jasiuk, 2018.

The second problem studied is simple tensile extension of a geometry including multiple Osteons, henceforth referred to as the "Multi-Osteon" geometry. The geometry was drawn from microscopy image from an actual donor specimen of human cortical bone³. The process of drawing the model is shown in Figure 3.7.

The Multi-Osteon problem inherits the material properties of the single Osteon problem, as well as the boundary conditions shown in Figure 3.8 below.

Idkaidek, Koric, and Jasiuk studied the Multi-Osteon model using meshes of six increasing densities. Only the results for the two least dense meshes are considered here. Two meshes of similar mesh densities were generated for this project. Table 4.3 summarizes the meshes considered for the Multi-Osteon case study.

	Idkaidek, Koric, and Jasiuk, 2018	Present Work
Coarse Mesh	4619 (quadrilateral bilinear elements)	5920 (triangular quadratic elements)
Refined Mesh	13,114 (quadrilateral bilinear elements)	13,711 (triangular quadratic elements)

Table 3.3: Meshes considered for the Multi-Osteon Case Study

Boundary conditions of 3 m, 5 m, and 10 m extension were used, and for the coarse mesh two different load increments of 0.05 and 0.01 were used to show temporal convergence. These results are shown in Figures 3.9 - 3.12.

³Idkaidek, Koric, and Jasiuk, 2018.

3 Cortical Bone Case Study

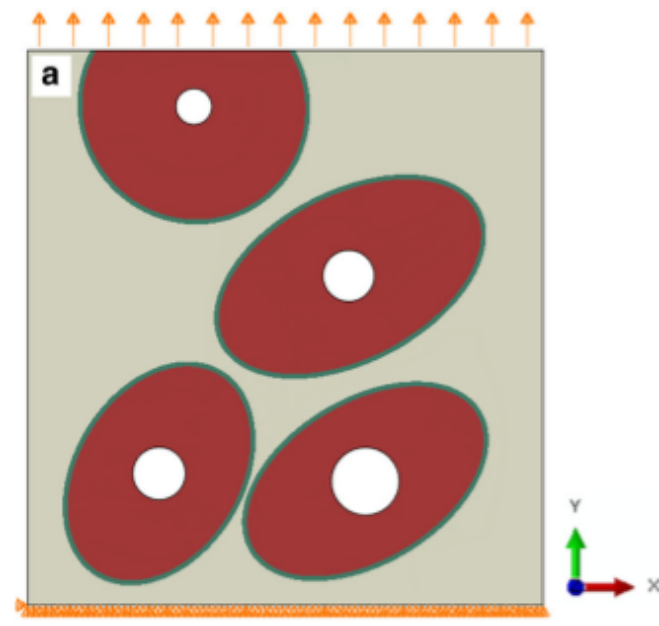


Figure 3.8: Schematics of Mixed Boundary Conditions Applied to Multi-Osteon Model. Reproduced from Idkaidek, Koric, and Jasiuk, 2018.

3.1 Simulation of Meso-scale Features: Osteons

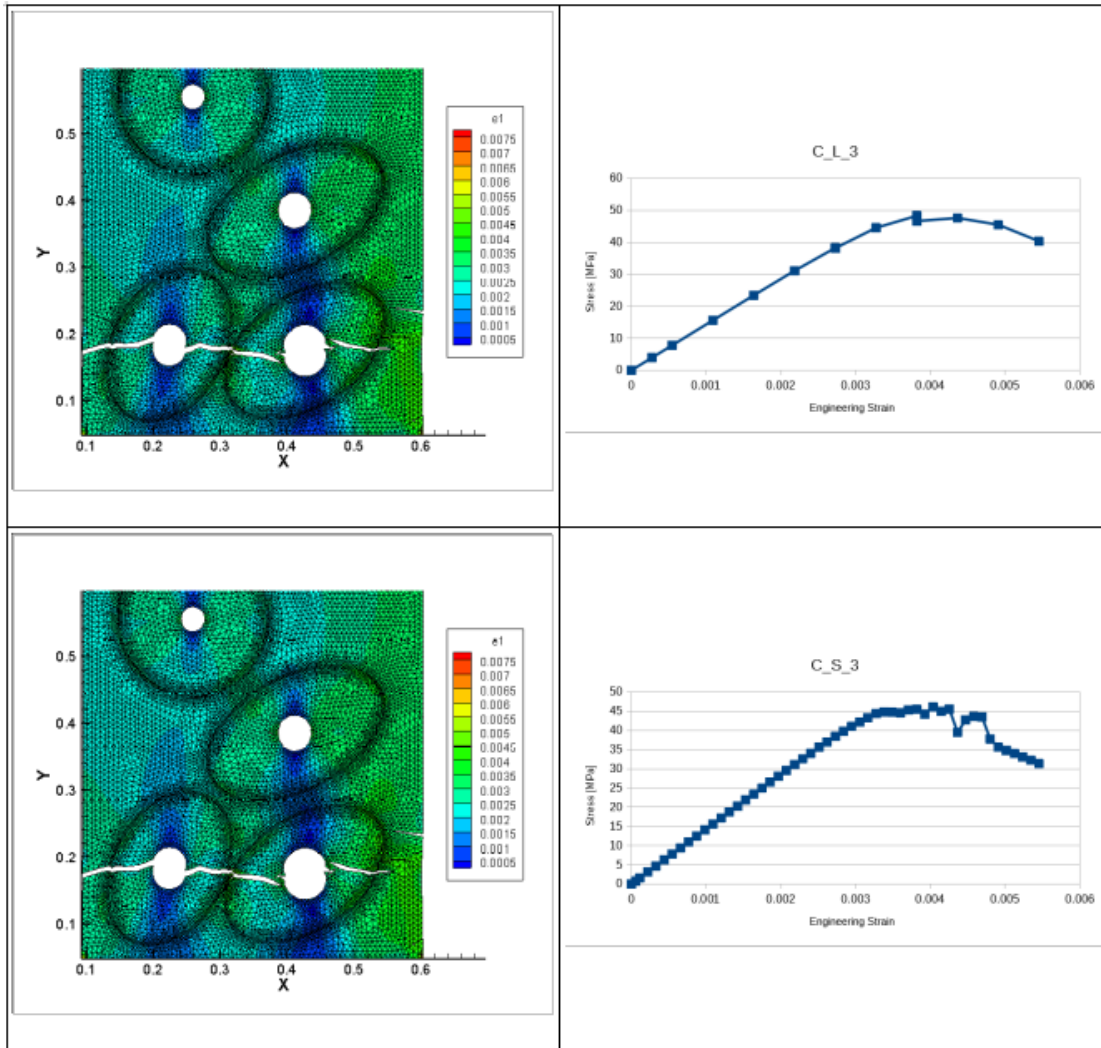


Figure 3.9: Results of Coarse Mesh Multi-Osteon Geometry; 3 μm Boundary Condition.
 Top row: Coarse mesh, with 3 μm extension, 0.05 step size (DEFSCALE=5)
 Bottom row: Coarse mesh, with 3 μm extension, 0.01 step size (DEFSCALE=5)

3 Cortical Bone Case Study

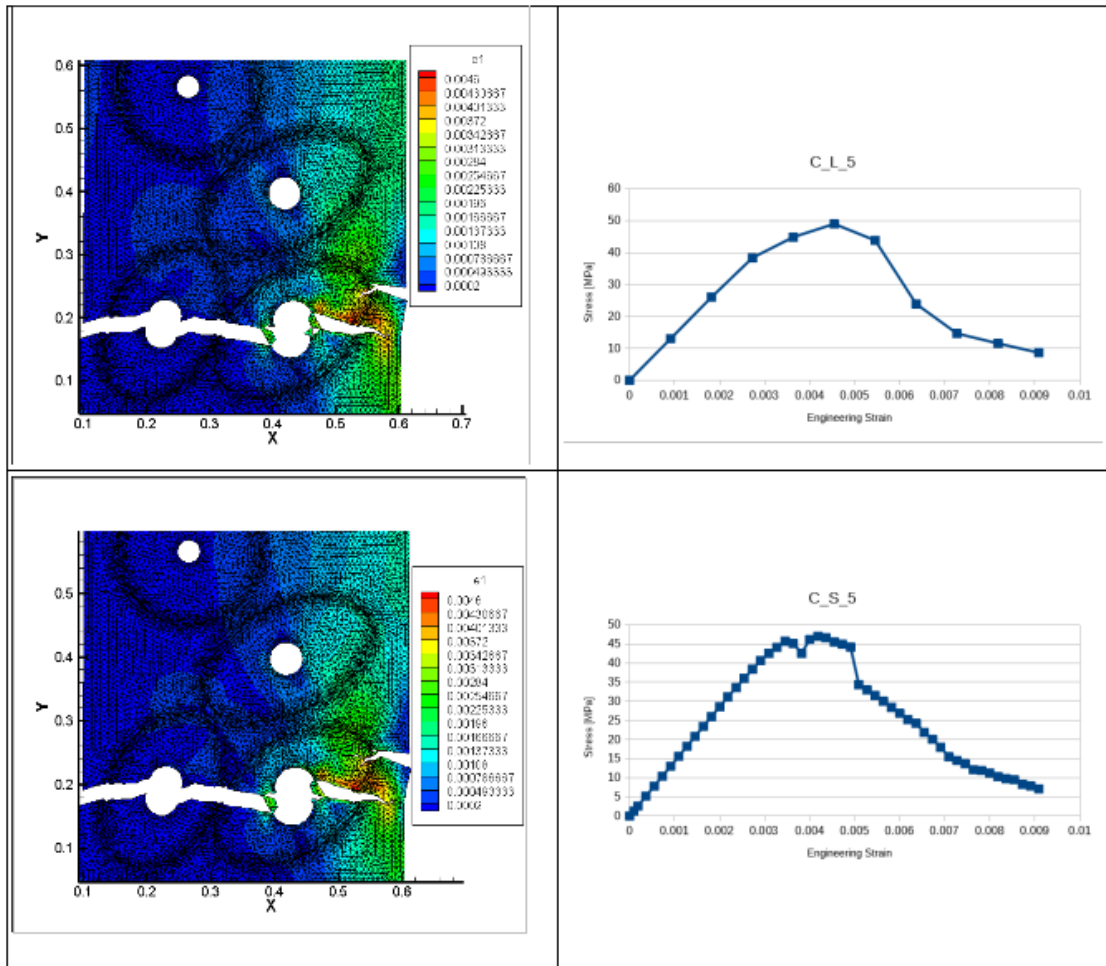


Figure 3.10: Results of Coarse Mesh Multi-Osteon Geometry; $5 \mu\text{m}$ Boundary Condition.
 Top row: Coarse mesh, with $5 \mu\text{m}$ extension, 0.05 step size (DEFSCALE=5)
 Bottom row: Coarse mesh, with $5 \mu\text{m}$ extension, 0.01 step size (DEFSCALE=5)

3.1 Simulation of Meso-scale Features: Osteons

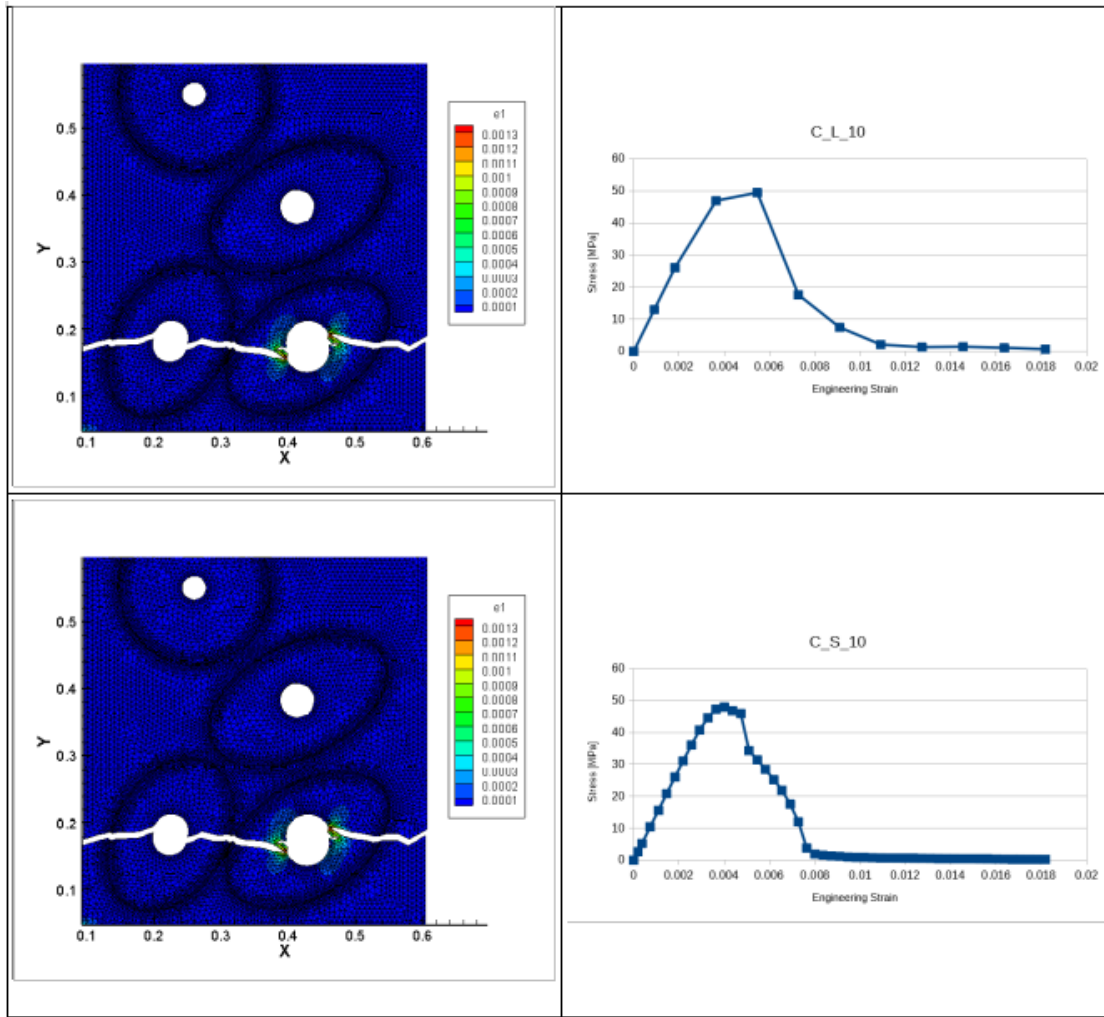


Figure 3.11: Results of Coarse Mesh Multi-Osteon Geometry; $10\ \mu\text{m}$ Boundary Condition.
 Top row: Coarse mesh, with $10\ \mu\text{m}$ extension, 0.05 step size (DEFSCALE=1)
 Bottom row: Coarse mesh, with $10\ \mu\text{m}$ extension, 0.01 step size (DEFSCALE=1)

3 Cortical Bone Case Study

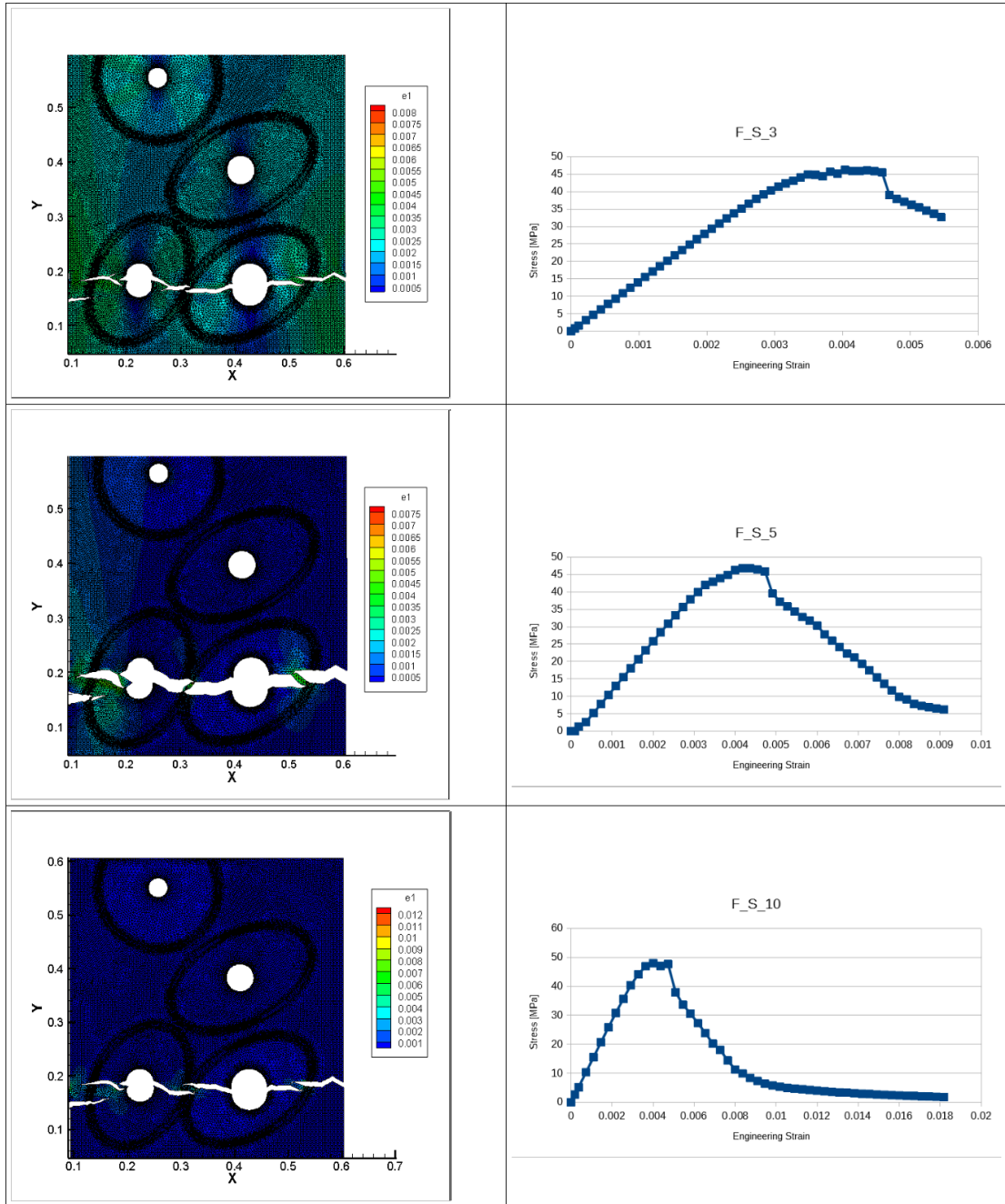


Figure 3.12: Results of Refined Mesh Multi-Osteon Geometry.

Top row: Refined mesh, with $3 \mu\text{m}$ extension, 0.01 step size (DEFSCALE=5)

Middle row: Refined mesh, with $5 \mu\text{m}$ extension, 0.01 step size (DEFSCALE=5)

Bottom row: Refined mesh, with $10 \mu\text{m}$ extension, 0.01 step size (DEFSCALE=1)

3.1 Simulation of Meso-scale Features: Osteons

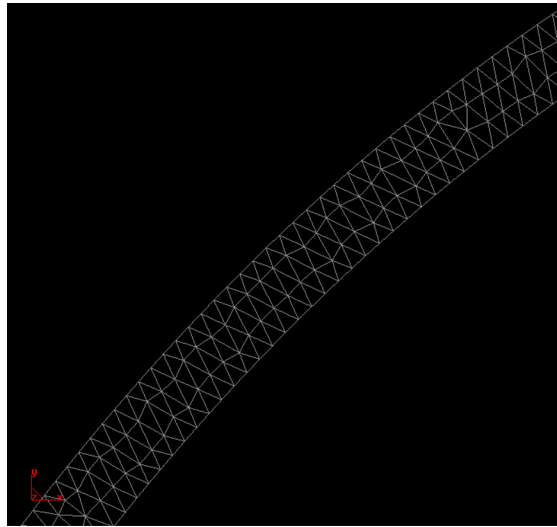


Figure 3.13: Example of meshed cement line with 3-element through the thickness of the cement-line.

In communication with Idkaidek and Jasiuk, it was decided that in order for the results of the present work to be more comparable to the XFEM method some revisions needed to be made to the meshes studied. In order to accurately capture the effect of the cement line, there must be 3 elements present through the thickness of the cement line such as in in Figure 3.13 .

Idkaidek prepared three new meshes meeting these requirements. Figures 3.14 - 3.15 present the results of $3\mu\text{m}$ extension using the energy based discrete fracture method. Future work will compare these results to the XFEM method which Idkaidek will provide.

Up to the known mesh dependence of the energy based discrete fracture method, comparable results are achieved for each mesh.

3 Cortical Bone Case Study

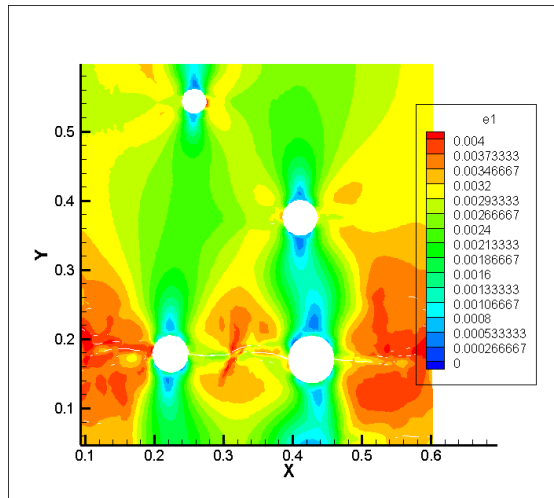


Figure 3.14: Principle strain contour for Multi-Osteon mesh with 5222 elements.
Mixed Boundary Conditions, $3 \mu\text{m}$.
3 elements through the thickness of the cement line.

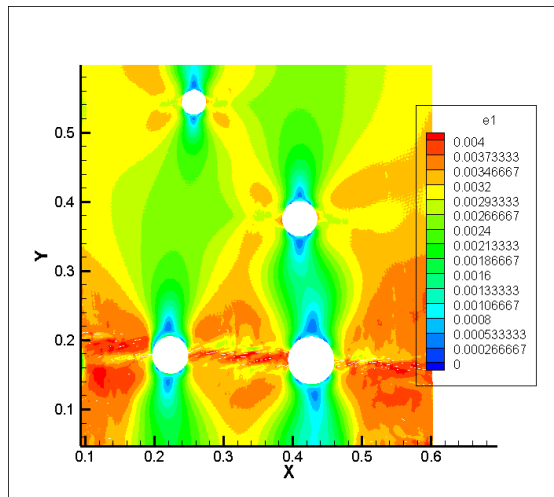


Figure 3.15: Principle strain contour for Multi-Osteon mesh with 24329 elements.
Mixed Boundary Conditions, $3 \mu\text{m}$.
3 elements through the thickness of the cement line.

3.2 Simulation of Macro-scale Problem: Beam with Notch

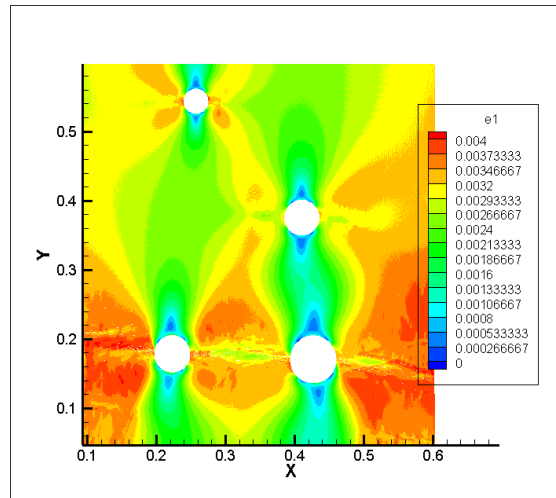


Figure 3.16: Principle strain contour for Multi-Osteon mesh with 68325 elements.
Mixed Boundary Conditions, $3 \mu\text{m}$.
3 elements through the thickness of the cement line.

3.2 Simulation of Macro-scale Problem: Beam with Notch

The macro-scale problem which has been studied by Professor Thomas Willet and his PhD Candidate Daniel Dapaah is the 3-point bending of a notched sample of human cortical bone⁴. The test configuration for this problem is shown in Figure 3.17.

After deforming the sample, a stained image was obtained to capture the region of the material that underwent damage. Dapaah and Willet refer to this region as the 'microdamage process zone'. The stained image, shown in Figure 3.18, shows in red all regions where the material has cracked and the dye used as filled the cracks.

⁴Dapaah, 2018.

3 Cortical Bone Case Study

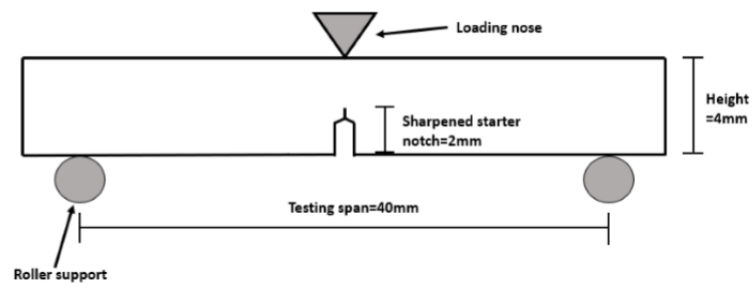


Figure 3.17: Test geometry for 3-point bend test of human cortical bone. Reproduced from Dapaah, 2018.

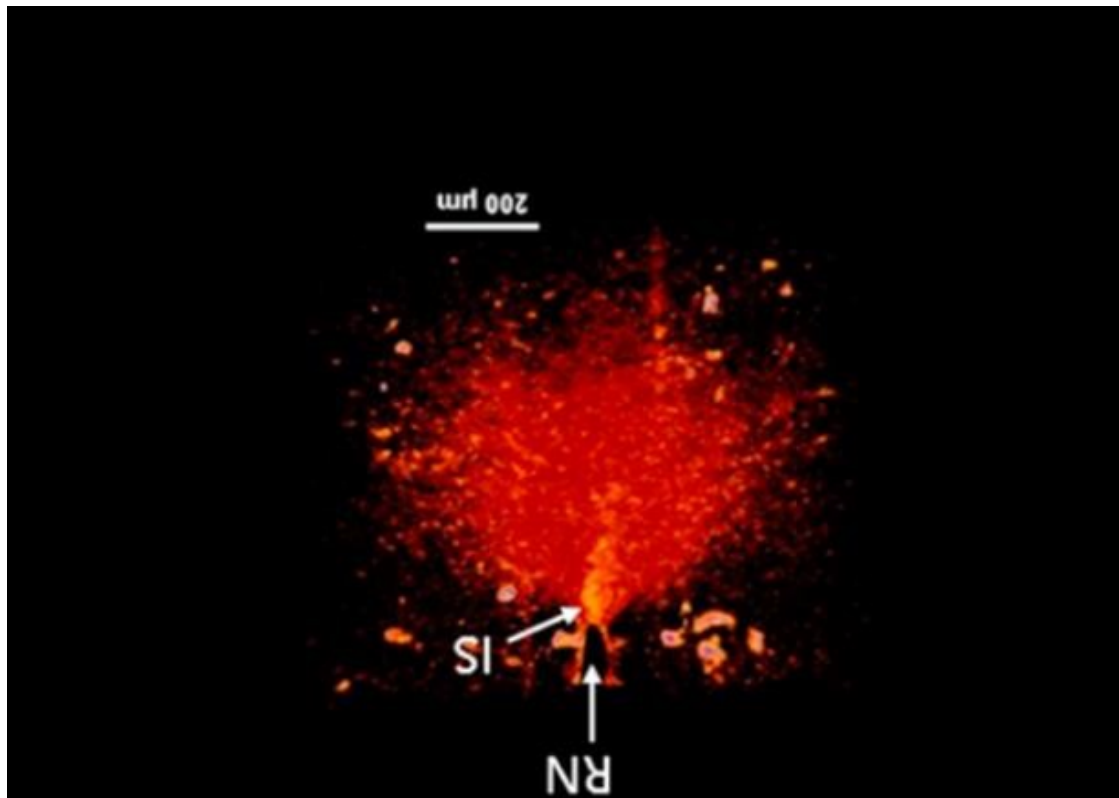


Figure 3.18: Results from imaging the microdamage process zone. Reproduced from Dapaah, 2018.

3.2 Simulation of Macro-scale Problem: Beam with Notch

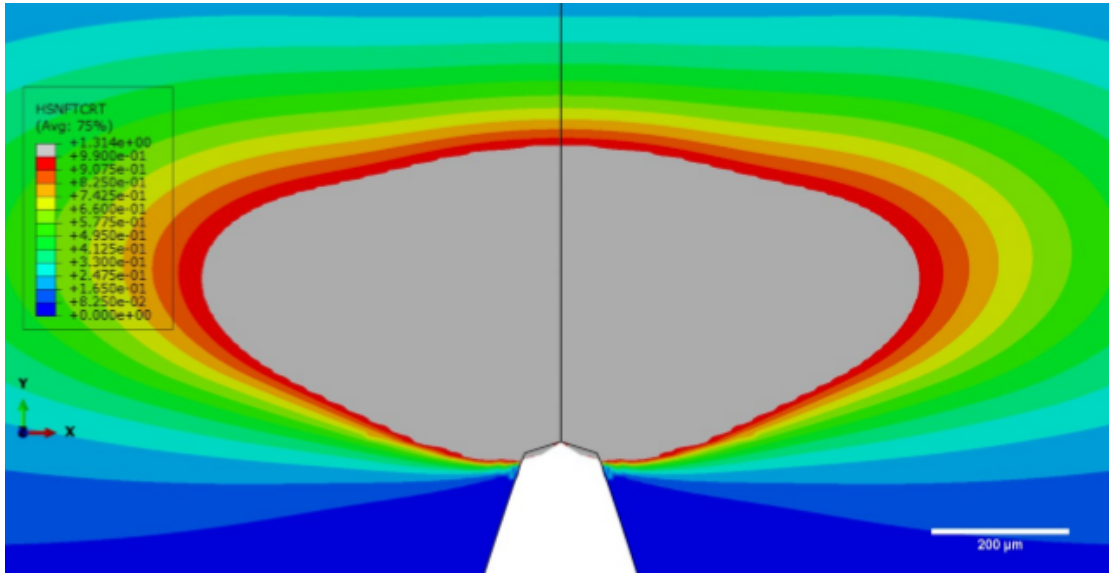


Figure 3.19: Microdamage process zone, contour produced from Hashin Fiber Composite model. Reproduced from Dapaah, 2018.

The Osteons studied in the macro-scale problem lay in along the horizontal-axis as fibers along the cortical bone sample. Then the macro-scale problem requires the cortical bone to be modeled as a transversely isotropic material. Daapha and Willet studied this problem using a Hashin continuum damage model for Fiber Composite materials in the commercial software ABAQUS.

Daapah and Willet represent the microdamage process zone in their model by calculating a damage parameter. The contour for the damage parameter is shown in Figure 3.19, regions where the damage parameter exceeds 1.0 (grey) are fully-damage, i.e. lay within the microdamage process zone where cracks in the material have opened.

In order to apply the energy based discrete fracture model, a general anisotropic extension of the base model was prepared.

The anisotropic extension results from a simple adjustment of the cohesive surface energy function. For material directions \vec{m}_1 and \vec{m}_2 , the cohesive surface energy function is decomposed as in equation 3.3.

$$\int_{\Gamma_d} \psi_{cohs}(\delta) dS = \int_{\Gamma_d} \psi_1(\delta_1) dS_1 + \int_{\Gamma_d} \psi_2(\delta_2) dS_2 \quad (3.3)$$

3 Cortical Bone Case Study

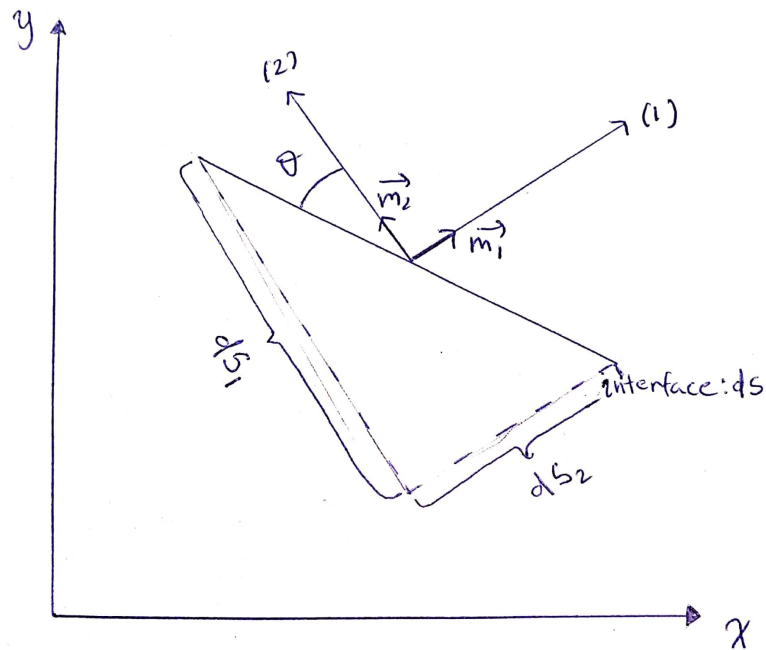


Figure 3.20: Differential elements along an interface with material directions \vec{m}_1 \vec{m}_2

Where dS_1 and dS_2 are differential elements across the projected from each interface perpendicular to the corresponding material direction, as in Figure 3.20.

Three test simulations were performed to validate the performance of the anisotropic extension to the model. In each test simulation a $100\text{mm} \times 100\text{mm}$ model was deformed under bi-axial tension by 0.5mm along both the horizontal and vertical axes. The material directions are such that the first material direction lines up with the horizontal axis, and the second material direction lines up with the vertical axis. In each test simulation failure is suppressed everywhere in the mesh except along a surface embedded in the mesh. In the first test simulation the surface is at a 30 degree incline to the horizontal axis, in the second and third test simulation the surface is at a 45 degree incline to the horizontal axis. Table 3.4 details the material properties for each test simulation. Figures 3.21 - 3.23 show the principal strain contour of the fully deformed meshes.

3.2 Simulation of Macro-scale Problem: Beam with Notch

	E_1 [GPa]	E_2 [GPa]	G_{12} [GPa]	σ_{c1} [MPa]	σ_{c2} [MPa]	G_{c1} [N/mm]	G_{c2} [N/mm]
First Test	59.2	59.2	4.34	200	200	22.5	22.5
Second Test	59.2	49.95	4.34	200	200	22.5	22.5
Third Test	59.2	59.2	4.34	200	100	22.5	11.25

Table 3.4: Anisotropic Material Properties used for Test Simulations

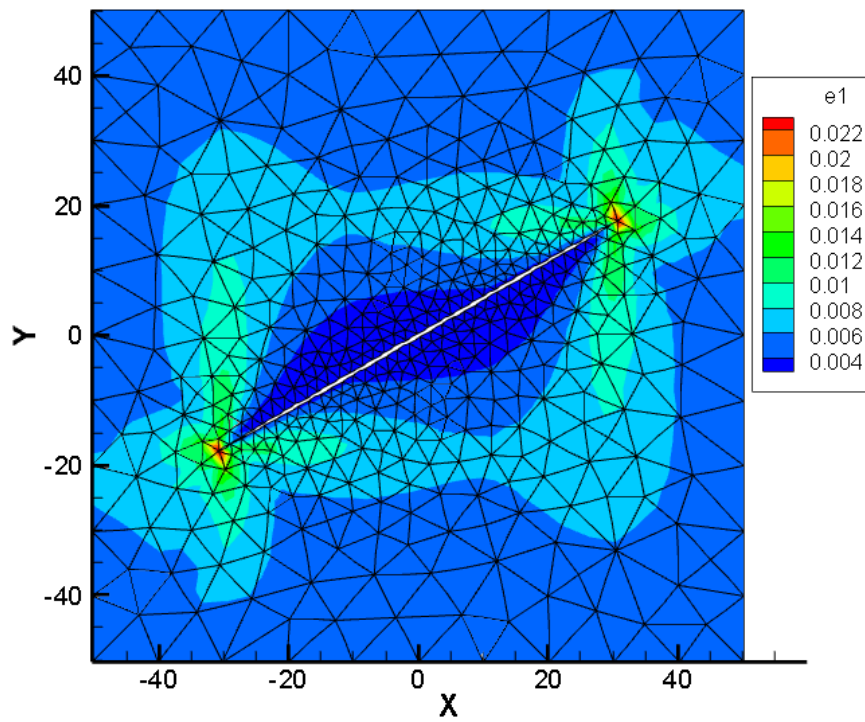


Figure 3.21: Principle Strain Contour of First Test Simulation for Anisotropic extension to Base Model.

3 Cortical Bone Case Study

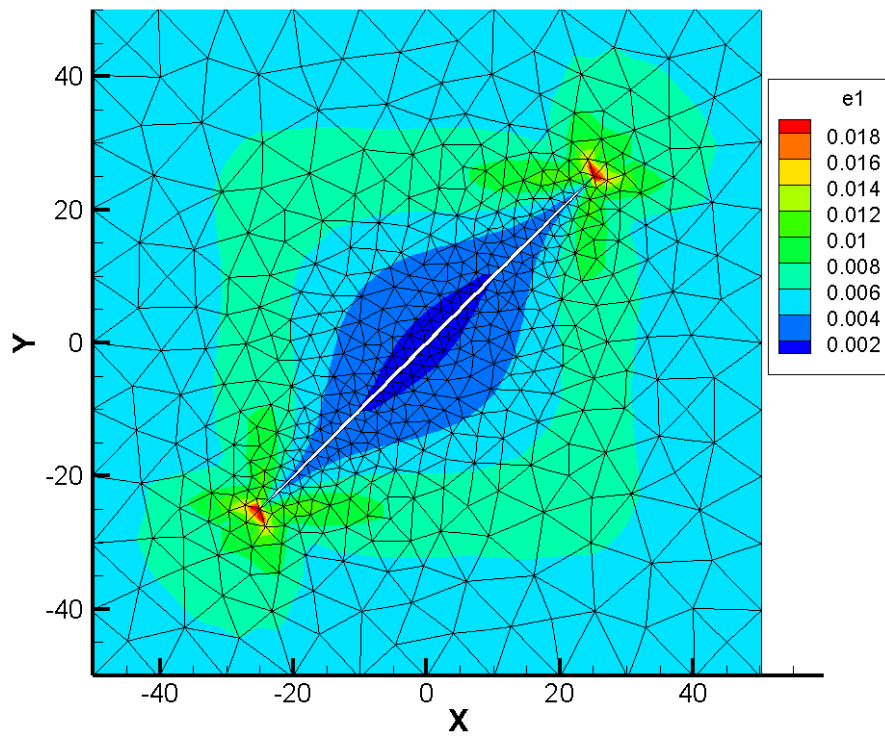


Figure 3.22: Principle Strain Contour of Second Test Simulation for Anisotropic extension to Base Model.

3.2 Simulation of Macro-scale Problem: Beam with Notch

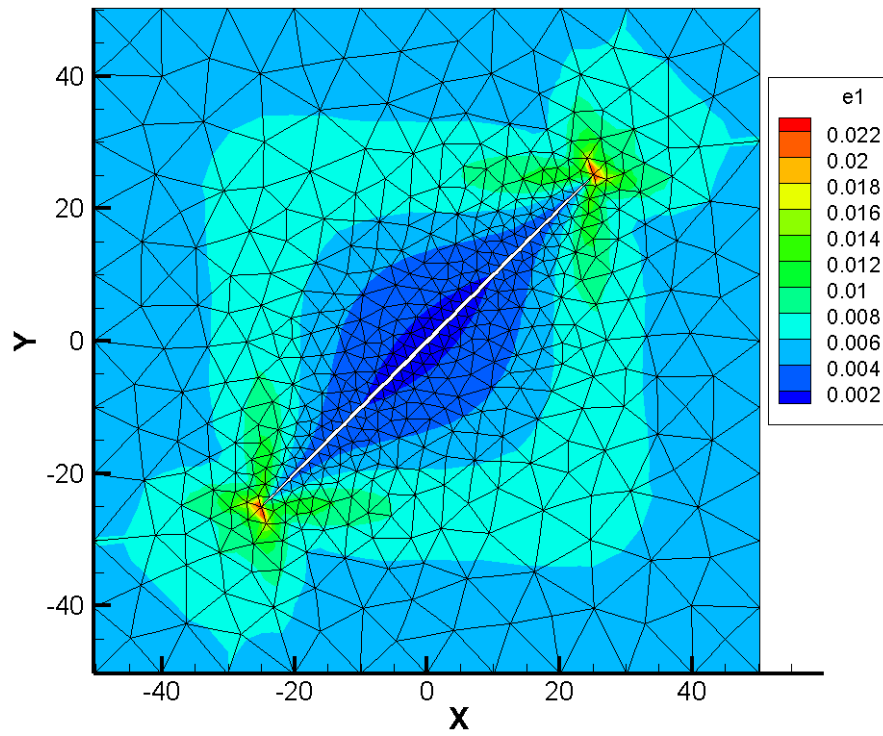


Figure 3.23: Principle Strain Contour of Third Test Simulation for Anisotropic extension to Base Model.

3 Cortical Bone Case Study

The force history for each test simulation can be analyzed to validate the performance of the anisotropic extension to the base method. The force history for the first test simulation is shown in Figure 3.24. The force history of the first test simulation shows the force increasing in both directions at the same rate pre-failure since the elastic modulus is the same in both material directions. Both directions fail at the same load since the cohesive strength is the same in each material direction. During failure, the force drops more in the second material direction due to the projected area of the embedded surface corresponding to the second direction being larger than the projected area corresponding to the first material direction.

The force history for the second test simulation is shown below in Figure 3.25. The force history of the second test simulation shows the force increasing at a slower rate pre-failure in the second direction since the elastic modulus is lesser in the second material direction than in the first material direction. The force drop during failure is the same in both directions and fail at the same load, since the fracture properties are the same in both material directions.

The force history for the third test simulation is shown below in Figure 3.26. The force history of the first test simulation shows the force increasing in both directions at the same rate pre-failure since the elastic modulus is the same in both material directions. The material fails in the second material direction at a load one-half of the load that the first material direction fails at since the cohesive strength in the second material direction is one half of the cohesive strength in the first material direction. The leveling off of the force in the second direction is attributed to the fact that the first direction is still undergoing elastic loading. Due to the Poisson effect there is a positive contribution to the stiffness in the second direction. The combination of failure in the second direction and the Poisson effect result in a near constant load during failure.

3.2 Simulation of Macro-scale Problem: Beam with Notch

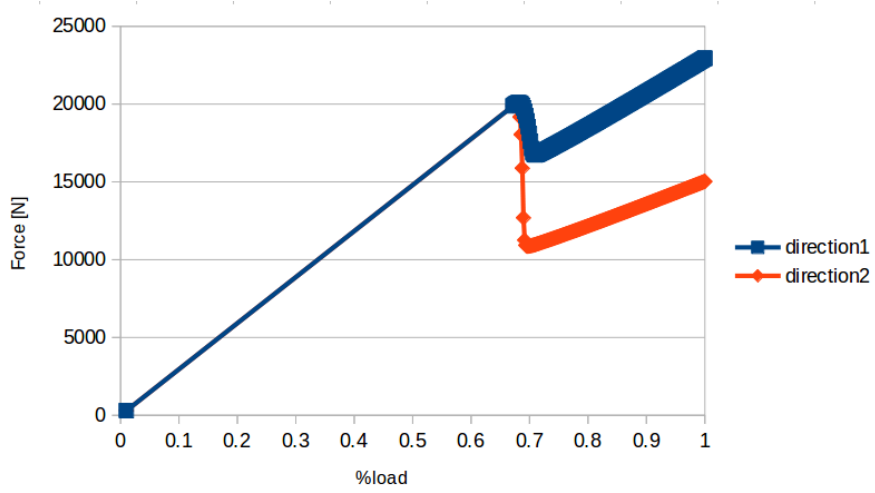


Figure 3.24: Force History of First Test Simulation for Anisotropic extension to Base Model.

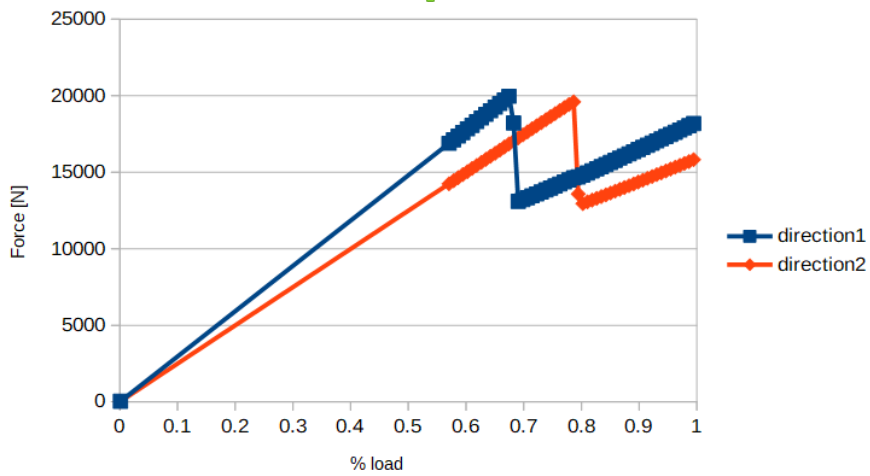


Figure 3.25: Force History of Second Test Simulation for Anisotropic extension to Base Model.

3 Cortical Bone Case Study

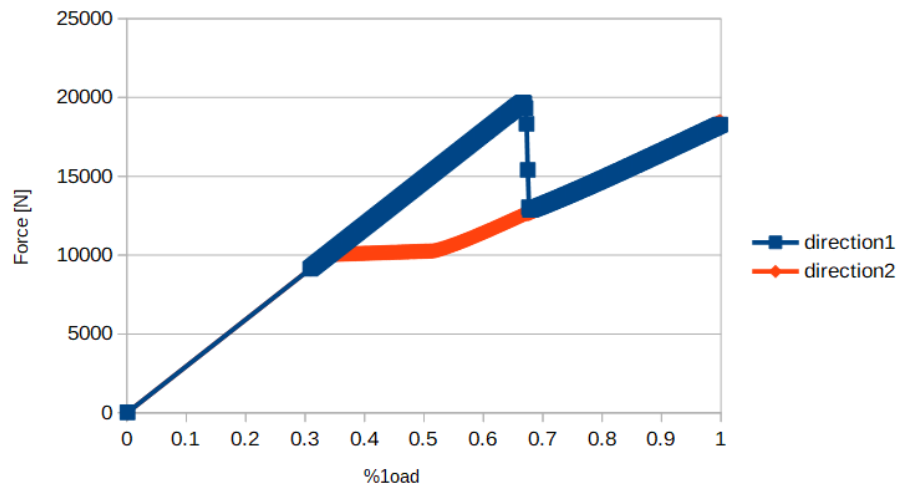


Figure 3.26: Force History of First Third Simulation for Anisotropic extension to Base Model.

The anisotropic extension the base method can be applied to macro-scale problem. The material properties for the macro-scale problem are presented in Table 3.5 below.

E_1 [GPa]	E_2 [GPa]	G_{12} [GPa]	σ_{c1} [MPa]	σ_{c2} [MPa]	G_{c1} [N/mm]	G_{c2} [N/mm]
18.3	9.9	4.1	80	40	0.004	0.0007

Table 3.5: Anisotropic Material Properties used for Macro-scale Problem

After applying 0.45mm of bending displacement to the model, the crack paths for the macro-scale problem is obtained. For the anisotropic extension, the crack paths are presented as the projections of the failed interfaces. When failure at an interface occurs in the first material direction a blue vertical line is plotted. When failure occurs in the second material direction a red horizontal line is plotted. The obtained crack paths are plotted in Figure 3.27.

The obtained crack path can be super-imposed on the experimental image of the microdamage process zone to show that the crack paths approximately line up with the damage shown in the experimental sample, see Figure 3.28.

3.2 Simulation of Macro-scale Problem: Beam with Notch

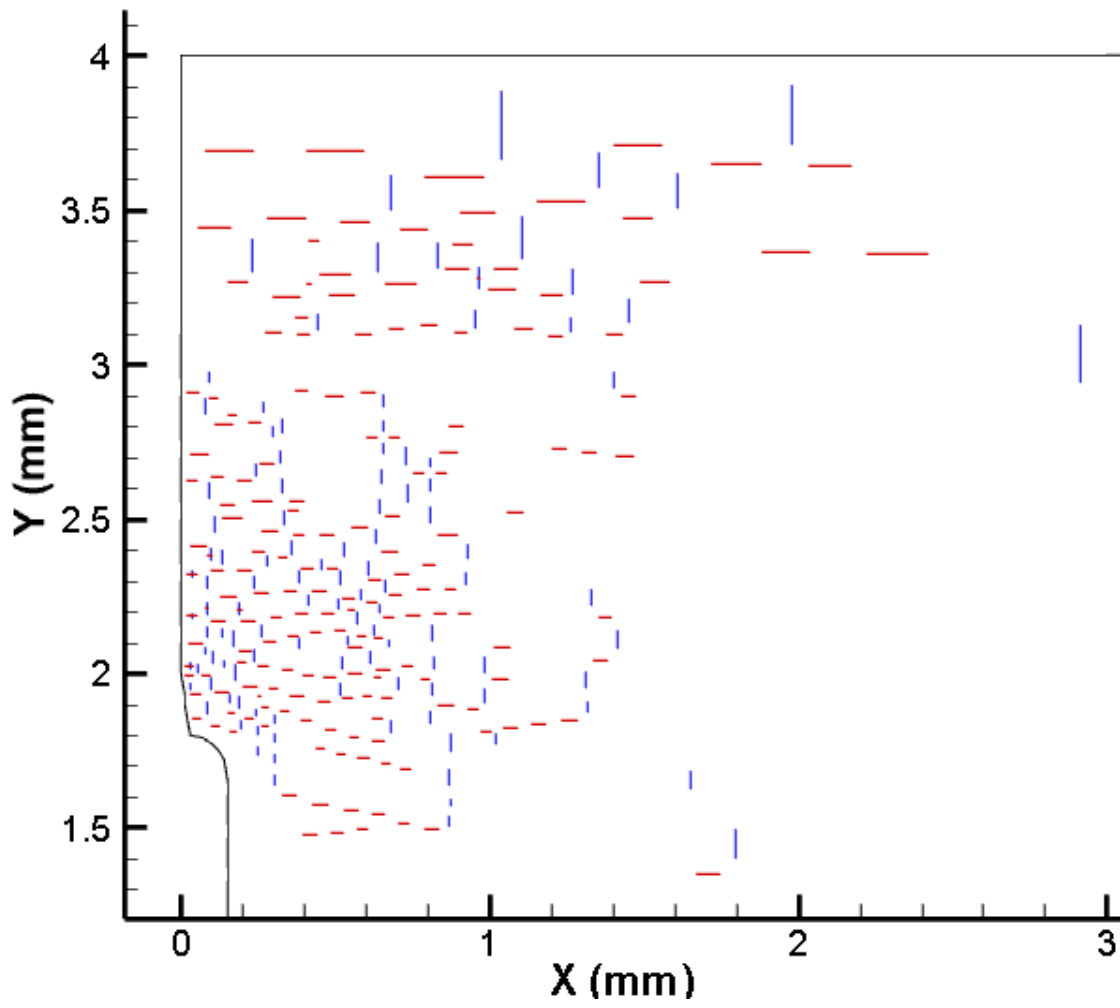


Figure 3.27: Crack paths obtained for Macro-scale problem using Anisotropic extension.

3 Cortical Bone Case Study

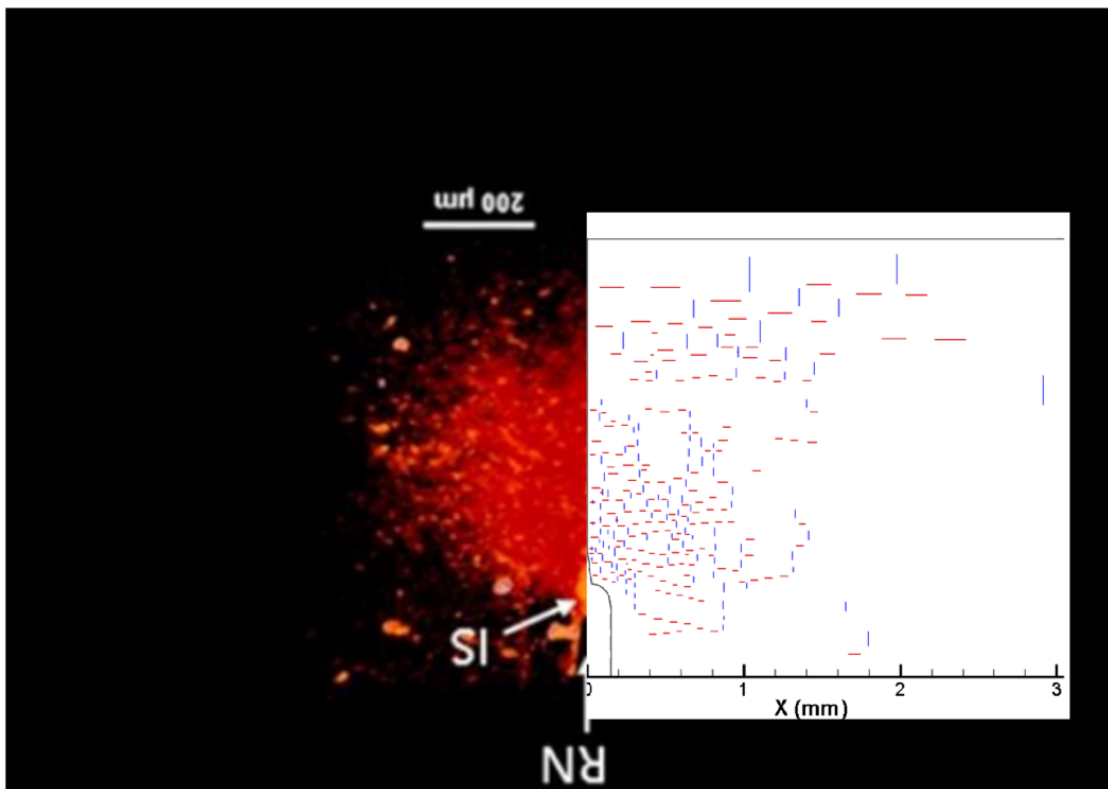


Figure 3.28: Crack paths obtained for Macro-scale problem using Anisotropic extension.

Bibliography

- Dapaah, Daniel (2018). "An experimentally validated continuum damage mechanics model of the micro-damage process zone during cortical bone fracture." MA thesis. Dept. of Engineering: University of Waterloo (cit. on p. 27).
- Hirmand, M. Reza and Katerina D. Papoulia (2019). "Block coordinate descent energy minimization for dynamic cohesive fracture." In: *Computer Methods in Applied Mechanics and Engineering* 354, pp. 663–688. ISSN: 0045-7825. DOI: <https://doi.org/10.1016/j.cma.2019.05.051>. URL: <http://www.sciencedirect.com/science/article/pii/S0045782519303305> (cit. on p. 3).
- Idkaidek, Ashraf and Iwona Jasiuk (2017). "Cortical bone fracture analysis using XFEM – case study." In: *International Journal for Numerical Methods in Biomedical Engineering* 33.4. e2809 CNM-Apr-16-0079.R1, e2809. DOI: 10.1002/cnm.2809. eprint: <https://onlinelibrary.wiley.com/doi/pdf/10.1002/cnm.2809>. URL: <https://onlinelibrary.wiley.com/doi/abs/10.1002/cnm.2809> (cit. on pp. 1, 13).
- Idkaidek, Ashraf, Seid Koric, and Iwona Jasiuk (2018). "Fracture analysis of multi-osteon cortical bone using XFEM." In: *Computational Mechanics* 62.2, pp. 171–184. ISSN: 1432-0924. DOI: 10.1007/s00466-017-1491-3. URL: <https://doi.org/10.1007/s00466-017-1491-3> (cit. on p. 19).
- Lawn, Brian (1993). *Fracture of Brittle Solids*. 2nd ed. Cambridge Solid State Science Series. Cambridge University Press. DOI: 10.1017/CB09780511623127 (cit. on p. 13).
- Ortiz, M. and A. Pandolfi (1999). "Finite-deformation irreversible cohesive elements for three-dimensional crack-propagation analysis." In: *International Journal for Numerical Methods in Engineering* 44.9, pp. 1267–1282. DOI: 10.1002/(SICI)1097-0207(19990330)44:9<1267::AID-NME486>3.0.CO;2-7. eprint: <https://onlinelibrary.wiley.com/doi/pdf/10.1002/%28SICI%291097-0207%2819990330%2944%3A9%3C1267%3A%3AAID-NME486%3E3.0.CO%3B2-7>. URL: <https://onlinelibrary.wiley.com/doi/abs/10.1002/%28SICI%291097-0207%2819990330%2944%3A9%3C1267%3A%3AAID-NME486%3E3.0.CO%3B2-7> (cit. on p. 6).

Bibliography

- Singh, Arjun (2018). *Cortical Bone and Cancellous Bone*. URL: boneandspine.com/cortical-bone-and-cancellous-bone/ (visited on 11/14/2017) (cit. on p. 1).
- Vashishth, Deepak (2007). "Hierarchy of bone microdamage at multiple length scales." In: *International Journal of Fatigue* 29.6, pp. 1024–1033. ISSN: 0142-1123. DOI: <https://doi.org/10.1016/j.ijfatigue.2006.09.010>. URL: <http://www.sciencedirect.com/science/article/pii/S0142112306002647> (cit. on p. 1).
- Wedro, Benjamin (2017). *Types of Bone Fractures: Healing Tailbone, Collarbone Others*. URL: www.medicinenet.com/broken_bone_types_of_bone_fractures/article.htm (cit. on p. 1).